Performance prediction of 1d Lobster eye X-ray optics for Astronomical observations.

Panini S. Singam[a,b], Philip Kaaret[b], Stephen D. Bongiorno[b], Danielle N. Gurgew[a,b], Tomasz M. Lis[b], Richard Yang[c,d], and Christian Captain[c,e]

[a]Universities Space Research Association Science and Technology Institute, Huntsville, Alabama, United States
[b]NASA Marshall Space Flight Center, Huntsville, Alabama, United States
[c]NASA OSTEM Intern, NASA Marshall Space Flight Center, Huntsville, Alabama, United States
[d]Georgia Institute of Technology, Atlanta, Georgia, United States
[e]Clemson University, Clemson, South Carolina, United States

ABSTRACT

Lobster eye optics enables wide-field X-ray telescope design that trades angular resolution for large field of view. This characteristic makes Lobster eye optic particularly suitable for time-domain and multi-messenger astrophysics applications. We present the development of a one-dimensional Lobster eye optic system at NASA Marshall Space Flight Center (MSFC) for wide-field X-ray monitoring missions. The proposed instrument incorporates over one thousand small flat reflecting surfaces arranged in cylindrical geometry to achieve approximately 20-degree field of view. Critical performance parameters include individual reflector geometry, surface flatness, profile errors, coating-induced stress, and alignment precision. We developed a wavelength-dependent ray-tracing algorithm that directly incorporates metrology and finite element method (FEM) data to quantify error contributions. The ray-trace simulations generate point spread function (PSF) characteristics and effective area calculations across the operating energy range (30 keV). We analyze how each error source degrades both the imaging performance and effective area of the system. This paper presents the 1D Lobster eye optic design configuration and comprehensive ray-trace analysis results demonstrating the error from the prescription and due to mirror and alignment imperfections. The modeling approach enables systematic optimization of Lobster eye optic performance for high-energy transient event monitoring applications.

Keywords: X-ray optics, lobster eye optics, ray tracing, error analysis, time-domain astronomy

1. INTRODUCTION

The Astro2020 Decadal Survey identifies Time Domain and Multi-Messenger Astrophysics (TDAMM) as the highest priority space-based sustaining activity for the coming decade. Wide-field X-ray monitoring represents an essential capability that must be implemented on smaller-scale missions to achieve the ambitious scientific goals outlined in this roadmap. The X-ray sky exhibits remarkable variability across temporal scales from seconds to years, harboring numerous transient sources of both galactic and extragalactic origin that demand continuous surveillance. Among the most physically significant transient phenomena, gamma-ray bursts (GRBs) demonstrate the critical importance of wide-field X-ray monitoring, with X-ray afterglows detected in approximately 90% of classical GRB events.[1] These afterglows provide superior localization accuracy compared to gamma-ray observations, enabling rapid identification of counterparts across the electromagnetic spectrum and facilitating detailed multi-wavelength studies of these extreme astrophysical events.[2]

The recent advent of gravitational wave astronomy has fundamentally transformed our approach to transient astrophysics, establishing multi-messenger observations as a cornerstone of modern discovery science. The

Further author information: (Send correspondence to P.S.)
P.S.: E-mail: srikanthpanini.singam@nasa.gov

detection of GW170817, produced by a binary neutron star merger, marked the first simultaneous observation of gravitational waves and electromagnetic radiation from the same cosmic event. The initial electromagnetic detection was made by the Fermi Gamma-ray Burst Monitor at energies above 10 keV, demonstrating that X-ray monitoring serves as a critical trigger for comprehensive multi-messenger follow-up campaigns.[3] However, the large 31 square degree gravitational wave error region necessitated extensive searches across multiple telescopes to identify the optical counterpart. Wide-field X-ray monitoring with improved angular resolution would dramatically enhance the efficiency of electromagnetic counterpart searches, enabling localization accuracies of approximately 1 arcminute that could be followed up with single pointings of optical and infrared telescopes.

Current X-ray monitoring capabilities rely primarily on coded mask instruments that sacrifice sensitivity for field of view coverage, or traditional Wolter telescopes that provide excellent angular resolution but are fundamentally limited to approximately less than half a degree field of view. This technological gap severely constrains our ability to conduct systematic surveys for high-energy transients and limits the effectiveness of rapid follow-up observations essential for multi-messenger astrophysics. The science requirements for next-generation wide-field X-ray monitors include: simultaneous coverage of large sky regions , angular resolution better than 5 arcminutes to enable efficient counterpart identification, sensitivity improvements of 10-100 times over existing non-focusing systems, and rapid response capabilities for time-critical observations of transient events. Additionally, the energy coverage must extend from soft X-rays through the hard X-ray band to approximately 30 keV to capture the full spectral evolution of transient phenomena and optimize detection of high-redshift sources where spectral features are redshifted to lower energies.

Lobster eye optics represents an elegant solution to the fundamental trade-off between field of view and angular resolution that constrains traditional X-ray telescope designs. The practical implementation of such systems has been extensively studied using various approaches including flat glass mirrors in Kirkpatrick-Baez configurations[4] and miniaturized Schmidt arrays.[5,6] Inspired by the compound eyes of lobsters, this optical approach utilizes numerous small flat reflecting surfaces arranged in spherical geometry to achieve simultaneous wide-field coverage and grazing incidence X-ray focusing. Unlike conventional Wolter telescopes that employ nested paraboloid-hyperboloid mirror pairs optimized for narrow fields, lobster eye systems can achieve fields of view exceeding a few 10s of degrees while maintaining just enough angular resolution for source localization. The design principle relies on grazing incidence reflections from multiple flat mirror segments, where each segment contributes to the overall collecting area while the spherical arrangement ensures that X-rays from different sky directions are focused to a common detector plane. This approach enables the construction of wide-field X-ray monitors with sensitivity improvements of 10-100 times over non-focusing coded mask systems, directly addressing the critical need for enhanced transient detection capabilities.

One-dimensional lobster eye optics, also known as Schmidt optics, offers significant advantages over two-dimensional implementations for transient astronomy applications. The 1D configuration employs perpendicular arrays of double-sided reflecting flats arranged in a cylindrical geometry, providing focusing in one dimension while maintaining wide-field coverage in the orthogonal direction. This design approach delivers superior sensitivity for short-duration transient events because each detector pixel views the entire length of the field of view in the non-focused direction, maximizing the photon collection efficiency for rapidly varying sources. Detailed sensitivity calculations demonstrate that for bright, short-duration phenomena where background noise is negligible, 1D optics provide optimal performance by maximizing source photon collection.[6] The manufacturing simplicity of 1D systems represents another crucial advantage, as they avoid the complex fabrication challenges associated with creating spherical shells of square holes required for 2D lobster eye implementations.[7] Current 2D systems suffer from manufacturing limitations where flat microchannel plates with square pores must be slumped to spherical shapes, introducing distortions in pore geometry and alignment that limit angular resolution to approximately 5 arcminutes. In contrast, 1D lobster eye systems can be constructed using precision flat reflecting elements with straightforward alignment requirements, enabling better angular resolution while maintaining the wide-field advantages essential for transient monitoring applications.

2. DESIGN OF 1D LOBSTER EYE OPTICS

The fundamental architecture of our 1D lobster eye optical system follows the Schmidt arrangement, where numerous flat reflecting surfaces are positioned along a cylindrical surface with a common focal axis, as illustrated

in Figure 1. The geometric design represents a careful optimization of multiple competing requirements including field of view coverage, angular resolution, effective area, and manufacturing feasibility. The optical configuration achieves wide-field X-ray imaging capabilities while maintaining sufficient angular resolution for precise source localization, making it ideally suited for transient astronomy applications requiring rapid sky coverage and accurate position determination.

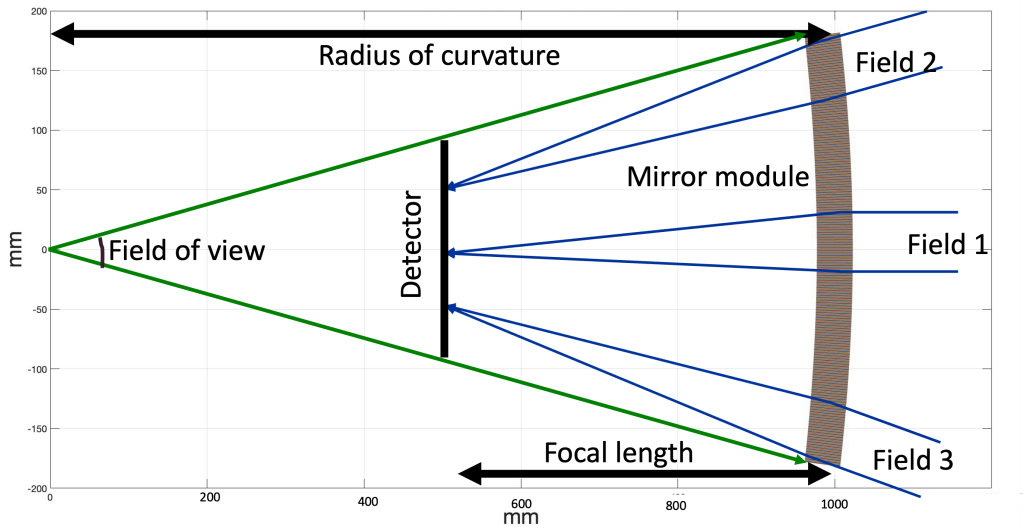

Figure 1: Schematic layout of the 1D lobster eye optical system showing the cylindrical arrangement of reflecting elements, focal length geometry, and field of view coverage. The radius of curvature is twice the focal length, and the detector is positioned at the focal plane to collect focused X-rays from different field angles.

The optical design is governed by several fundamental parameters that define the system geometry and performance characteristics, as depicted in Figure 1. We adopt a focal length of 500 mm, which corresponds to half the radius of curvature according to the Schmidt arrangement geometry shown in the schematic. This focal length provides an optimal balance between achieving the desired field of view coverage while maintaining practical system dimensions suitable for space-based deployment. The 500 mm focal length enables sufficient detector size accommodation while keeping the overall instrument envelope within reasonable spacecraft constraints. The detector configuration defines the active imaging area and directly determines the achievable field of view. The detector size along the imaging axis measures 180 mm, establishing the fundamental aperture through which focused X-rays are collected. This detector dimension, combined with the 500 mm focal length, creates the geometric foundation for the wide-field imaging capabilities shown in Figure 1. In the non-imaging direction, the detector maintains the same 270 mm dimension, maximizing the collection efficiency for the focused beam.

The individual reflecting elements represent the core optical components that enable the focusing capabilities. Each reflector has a thickness of 0.1 mm and the opening aperture between adjacent reflectors measures 0.2 mm, creating the fundamental spacing that determines both the angular resolution and the effective area characteristics. This aperture dimension establishes the basic cell structure that governs the optical performance across the entire energy range of interest. The reflector thickness and aperture spacing together define the packing efficiency and determine the fraction of incident X-rays that can be effectively focused onto the detector. The field of view emerges as a direct consequence of the detector dimensions and focal length through the fundamental geometric relationship FOV = $2\times\arctan(d/2f)$, where d represents the detector size and f the focal length. With our adopted parameters of d = 180 mm and f = 500 mm, this relationship yields a field of view of 20.4 degrees, as illustrated by the green field of view lines in Figure 1. The acceptance angle parameter defines the maximum grazing incidence angle at which X-rays can effectively undergo reflection within the individual cells. We establish an acceptance angle of 0.5 degrees, optimized for the operating energy range and reflective coating properties. This acceptance angle represents a compromise between maximizing the effective area at high

energies where critical angles are small, and maintaining reasonable throughput at lower energies where larger acceptance angles are beneficial. The acceptance angle directly influences the cell geometry and determines the relationship between cell dimensions and optical performance.

The cell height represents a critical derived parameter that governs the effective area characteristics and determines the physical extent of individual reflecting elements. The cell height follows the relationship h = a/tan(acceptance angle), where a represents the opening aperture and the acceptance angle defines the maximum useful grazing angle. With our design parameters of a = 0.2 mm and acceptance angle = 0.5 degrees, this relationship yields a cell height of 22.91 mm. If the physical height of the reflectors are larger than this, then they undergo vignetting for this acceptance angle requirement. This height ensures that X-rays entering the cell at the maximum acceptance angle can undergo proper reflection while maintaining adequate geometric throughput.

The complete optical system incorporates 1187 individual reflecting elements arranged in the cylindrical Schmidt geometry, as shown in the mirror module section of Figure 1. This large number of cells ensures adequate sampling of the spherical wavefront while providing sufficient effective area for astronomical observations. Each cell functions as an independent optical element, contributing to the overall system performance through coherent addition of reflected X-rays from different sky directions. The radius of curvature, measuring 1000 mm as indicated in Figure 1, establishes the fundamental spherical geometry that enables wide-field focusing capabilities. This curvature represents twice the focal length according to the Schmidt arrangement, creating the geometric relationship that allows X-rays from different field angles (Field 1, Field 2, and Field 3 as shown in the schematic) to converge at the detector plane. The spherical surface ensures that reflections from cells at different angular positions contribute constructively to the focused image, while the cylindrical symmetry in the non-imaging direction provides the one-dimensional focusing characteristic that distinguishes this design from traditional 2D lobster eye systems.

3. EFFECTIVE AREA ESTIMATION

3.1 Vignetting Effects in 1D Lobster Eye Optics

The estimation of effective area in lobster eye optics requires careful consideration of vignetting effects that arise from the close spacing of individual mirror elements. In our design configuration with an acceptance angle of 0.5 degrees, the geometric arrangement of reflecting surfaces creates natural shadowing between neighboring segments that significantly impacts the contributing area for any given field angle. This vignetting phenomenon represents a fundamental characteristic of the Schmidt arrangement and must be accurately accounted for in performance predictions.

Figure 2 illustrates the spatial distribution of vignetting effects across the mirror array for a representative field angle. The close placement of mirror elements naturally blocks on-axis X-rays for larger grazing angles, creating distinct regions of varying contribution efficiency. Cells located near the optical axis (green arrow region) experience full illumination and contribute their complete geometric area to the effective collection. These mirrors receive unobstructed X-ray flux and provide maximum reflection efficiency within the design acceptance angle. The intermediate region (purple arrow region) contains partially contributing cells where neighboring mirror elements create partial shadowing effects. These mirrors experience reduced effective height due to geometric obstruction from adjacent cells, resulting in diminished but non-zero contribution to the total effective area. The partial vignetting creates a gradual transition zone between fully contributing and completely blocked regions, with the degree of obstruction depending on the specific field angle and mirror position relative to the optical axis. Mirrors located beyond a critical angle threshold (red arrow region) become completely shadowed by their neighbors and contribute zero effective area for the given field configuration. These fully blocked cells experience complete geometric obstruction where neighboring elements entirely prevent incident X-rays from reaching the reflecting surface. However, these same mirrors may contribute significantly to effective area calculations for different field angles, demonstrating the field-dependent nature of the vignetting pattern.

For our current design configuration incorporating 1187 total mirror cells, only 117 cells contribute meaningful effective area for any given field angle. This represents approximately 10% of the total mirror population, with the remaining 90% completely vignetted for the specific field under consideration. The dramatic reduction

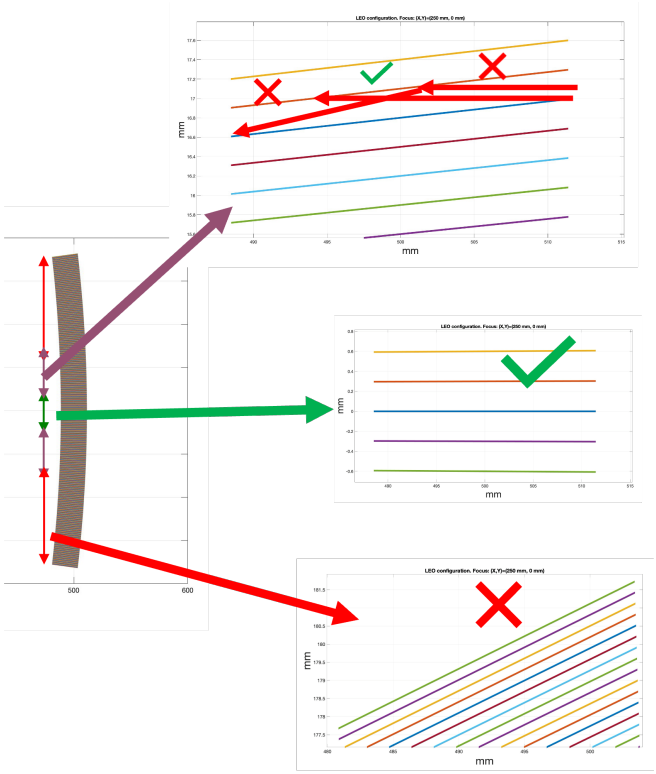

Figure 2: Vignetting effects in the 1D lobster eye configuration showing the contribution of different mirror cells to the effective area. Green regions indicate fully contributing cells, purple regions show partially contributing cells affected by neighboring shadows, and red regions represent fully blocked cells where neighboring elements completely obstruct incident X-rays.

in contributing elements emphasizes the importance of accurate vignetting calculations in predicting system performance and highlights the trade-offs inherent in the Schmidt optical arrangement. This field-dependent contribution pattern must be carefully integrated into effective area calculations to ensure accurate performance predictions across the full 20.4-degree field of view.

3.2 Effective Geometric Length of Mirror Elements

The effective area contribution from individual mirror cells depends not only on vignetting effects but also on the geometric projection of each mirror element relative to the incident X-ray direction. This geometric projection creates a fundamental trade-off between vignetting losses and effective mirror length that varies systematically across the mirror array. The effective height of each mirror cell can be quantified through the relationship:

$$Eh_i = h \cdot \sin(\theta_i) \cdot b_i \tag{1}$$

where h represents the physical height of the mirror cell, θ_i is the grazing angle for the i-th cell, and b_i is the blocking factor that accounts for vignetting effects from neighboring elements. Understanding this relationship is essential for accurate effective area calculations and reveals the complex interplay between optical geometry and collection efficiency in the Schmidt arrangement.

Mirror cells positioned close to the optical axis experience minimal vignetting ($b_i \approx 1$) but suffer from very small grazing angles θ_i relative to the incident field direction. The mirror located exactly on the optical axis exhibits zero effective projection length because $\sin(\theta_i) = 0$. As the distance from the optical axis increases, the $\sin(\theta_i)$ term grows systematically, creating a progressive increase in projected area for cells positioned farther from the central axis, provided the blocking factor remains near unity.

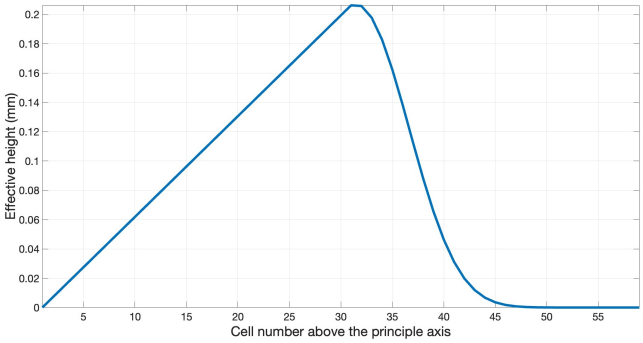

Figure 3: Effective height of mirror cells as a function of position above the optical axis. The curve shows the geometric projection effect where cells near the axis have minimal effective height due to small grazing angles, while cells farther from the axis achieve maximum effective height before vignetting effects cause rapid reduction.

Figure 3 demonstrates this geometric relationship by plotting the effective height of mirror cells as a function of their position above the optical axis. The curve exhibits a characteristic asymmetric profile that reflects the competing influences of the geometric projection term $\sin(\theta_i)$ and the vignetting-dependent blocking factor b_i. Cells closer to optical axis show a steady increase in effective height as the grazing angle increases, with the geometric projection dominating the calculation while b_i remains close to unity. This region represents the transition from zero effective area at the optical axis to progressively larger contributions as the sine of the grazing angle increases. The maximum effective height occurs around cell number 25-30 on either sides of the principle axis, where the optimal balance between the increasing $\sin(\theta_i)$ term and the still-favorable blocking factor b_i is achieved. At this position, the geometric projection has increased substantially from the on-axis condition, while vignetting effects have not yet significantly reduced the blocking factor. This peak represents the most efficient region of the mirror array where individual cells contribute their maximum effective area to the overall collection efficiency.

Beyond the peak position, cells numbered 30-50 experience rapidly decreasing effective height despite having larger grazing angles θ_i. This reduction results from the dramatic decrease in the blocking factor b_i as neighboring mirror elements begin to cast shadows that partially or completely obstruct the incident X-ray flux. The steep decline in effective height demonstrates how vignetting losses (decreasing b_i) eventually overwhelm the benefits of increased geometric projection (increasing $\sin(\theta_i)$), leading to negligible contributions from cells positioned far from the optical axis. This behavior confirms that only a subset of the total mirror population contributes meaningfully to the effective area for any given field angle, with the optimal contributing region determined by the balance between geometric projection and shadowing effects.

3.3 Energy-Dependent Effective Area Calculation

The calculation of effective area requires consideration of the energy-dependent X-ray reflectivity characteristics that vary systematically with grazing angle across the mirror array. X-ray reflection from metallic surfaces exhibits a characteristic energy-dependent relationship determined by the critical angle, which defines the maximum grazing angle under which X-ray reflectivity is possible for a particular wavelength. Beyond this critical angle, reflectivity drops to zero, creating sharp energy cutoffs that depend on both the material properties and the local grazing angle. Mirrors positioned at small grazing angles exhibit broad-band reflectivity extending to high energies, while mirrors at larger angles confine their reflectivity to progressively lower X-ray energies. The use of high-density reflective coatings extends the higher energy cutoff for any given angle, which motivates our selection of gold-coated mirrors for this application.

Figure 4 displays the energy-dependent reflectivity curves for all contributing mirror cells equipped with gold coatings. The multiple curves demonstrate the systematic variation in spectral response across the mirror array, with mirrors closer to the optical axis (smaller grazing angles) maintaining high reflectivity to energies exceeding 25 keV, while mirrors positioned farther from the axis show progressively lower energy cutoffs. The characteristic absorption edges of gold are visible around 2.2 keV and 11.9 keV, appearing as sharp features in the reflectivity

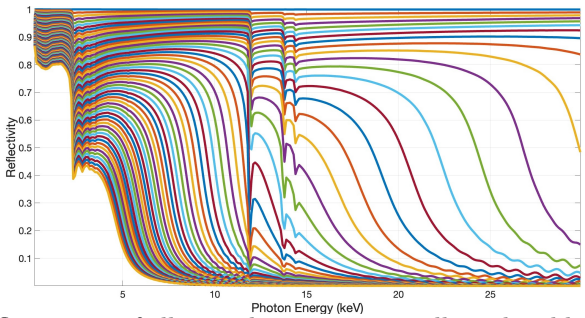

Figure 4: Energy-dependent reflectivities of all contributing mirror cells with gold coatings. Each curve represents a different mirror cell, showing the trend of higher energy cutoffs for mirrors at smaller grazing angles (upper curves) and progressively lower energy cutoffs for mirrors at larger grazing angles (lower curves).

curves. This energy-dependent behavior directly impacts the effective area contribution from each mirror cell and creates the wavelength-dependent performance characteristics of the overall system.

The effective area contribution from individual mirror cells requires the integration of reflectivity properties with geometric considerations through the relationship:

$$EA_i = R_i(\lambda) \cdot Eh_i \cdot w \tag{2}$$

where $R_i(\lambda)$ represents the energy-dependent reflectivity of the i-th mirror cell, Eh_i is the effective height calculated from geometric and vignetting considerations, and w is the mirror width in the non-imaging direction that provides a constant scaling factor. This formulation captures the fundamental physics where the collecting area depends on both the probability of reflection (determined by material properties and grazing angle) and the geometric cross-section available for X-ray collection.

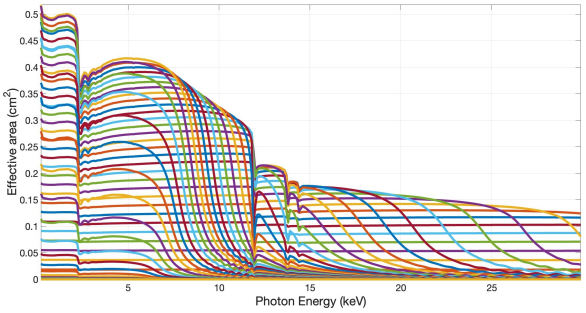

Figure 5: Effective area contributions from individual mirror cells as a function of photon energy. Cells closer to the optical axis exhibit lower but broad-band effective area, while cells farther from the axis show higher peak effective area confined to lower energies due to critical angle limitations.

Figure 5 illustrates the effective area contribution from each individual mirror cell across the operating energy range. The curves demonstrate the trade-off between broad-band coverage and peak effective area, with mirrors close to the optical axis providing modest but consistent contribution across the full energy range, while mirrors positioned at larger grazing angles contribute significantly higher peak areas but only at lower energies. The systematic progression of curves reflects the interplay between increasing effective height (due to larger grazing angles) and decreasing energy cutoffs (due to critical angle limitations). This behavior creates a complementary coverage pattern where different mirror cells dominate the effective area at different energies.

The total system effective area emerges from the coherent sum of contributions from all mirror cells according to:

$$EA = \sum_{i=1}^{N} [R_i(\lambda) \cdot w \cdot Eh_i] \tag{3}$$

where the summation extends over all N contributing mirror cells for the given field angle. This calculation accounts for the complex interplay between geometric projection, vignetting effects, and energy-dependent reflectivity to produce the overall system performance.

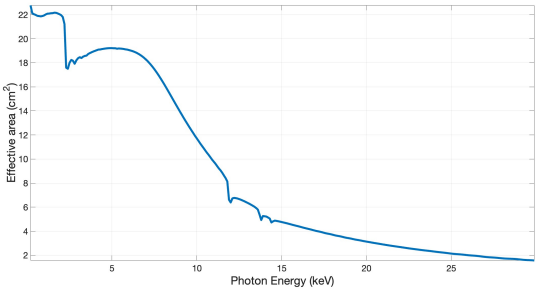

Figure 6: Total effective area of the 1D lobster eye system as a function of photon energy, showing the integrated contribution from all mirror cells. The curve exhibits high effective area at low energies with systematic reduction toward higher energies due to critical angle limitations.

Figure 6 presents the final effective area performance of the complete 1D lobster eye system. The characteristic energy dependence shows peak effective area of approximately 22 cm^2 at the lowest energies, with a gradual decline as energy increases due to the progressive loss of contributing mirror cells as their critical angles are exceeded. Notable features include the relatively flat response between 2-4 keV and the systematic reduction above 8 keV where only the most favorably positioned mirror cells continue to contribute. The absorption edge features from the gold coating appear as modulations in the overall curve, demonstrating the material-dependent aspects of the reflectivity characteristics. This effective area performance enables sensitive observations across the 1-10 keV energy range while maintaining substantial collecting power for the detection of high-energy transients.

4. IMAGING PERFORMANCE OF 1D LOBSTER EYE OPTICS

4.1 Fundamental Imaging Limitations from Flat Mirror Geometry

The imaging performance of 1D lobster eye optics is fundamentally constrained by the use of flat mirror elements to approximate the ideal spherical focusing surface. Unlike traditional X-ray telescopes that employ curved mirrors with intrinsic focusing power, the 1D Lobster eye optic design utilizes flat reflecting surfaces arranged in a spherical grid pattern. This geometric approximation introduces systematic imaging errors that vary across the mirror array and directly impact the achievable point spread function characteristics.

The absence of convergence in the axial direction of each flat mirror element creates a natural limitation in imaging quality, where the contribution to point spread function blur is directly proportional to the effective height of individual mirror cells. This relationship establishes a fundamental trade-off between effective area and imaging performance, as mirrors with larger effective heights contribute more photons to the focused image while simultaneously introducing greater geometric blur. The imaging error scales systematically with the projection area, creating position-dependent performance characteristics across the mirror array.

Figure 7 demonstrates this fundamental relationship by comparing the PSF spread contributions from two representative cases. Mirrors positioned close to the optical axis with small grazing angles produce minimal image blur due to their reduced effective projection area, as shown in the left panel. The compact PSF contribution reflects the limited geometric extent over which these mirrors collect incident X-rays. Conversely, mirrors located farther from the optical axis experience larger grazing angles that create substantially increased effective heights, resulting in correspondingly larger image blur contributions shown in the right panel. The extended PSF spread

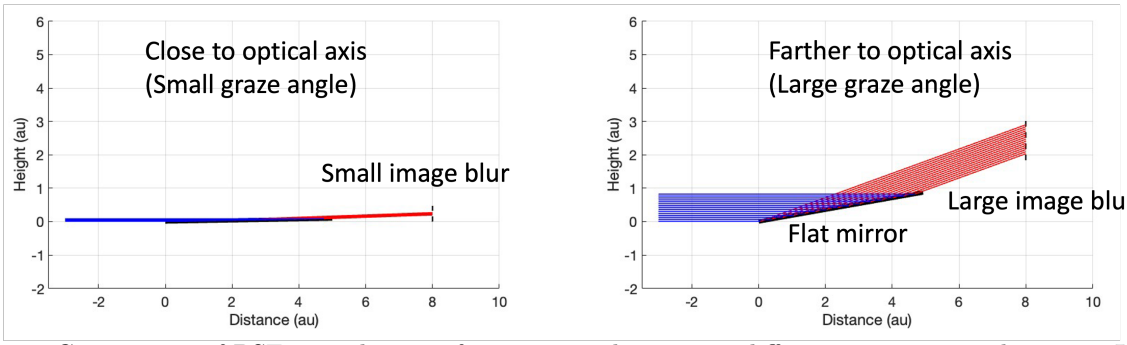

Figure 7: Comparison of PSF contributions from mirror elements at different positions in the array. Left panel shows the small image blur from mirrors close to the optical axis with small grazing angles, while the right panel demonstrates the large image blur from mirrors farther from the optical axis with large grazing angles and correspondingly larger effective projections.

directly reflects the larger geometric projection and the inherent limitation of using flat reflecting surfaces to approximate spherical focusing.

This position-dependent imaging behavior creates energy-dependent PSF characteristics, since different mirror cells dominate the effective area at different photon energies. At lower energies where mirrors across the full array contribute, the PSF incorporates blur contributions from both small and large effective height mirrors. At higher energies where only mirrors near the optical axis remain effective due to critical angle limitations, the PSF becomes dominated by the smaller blur contributions from low-projection mirrors. This systematic variation establishes the fundamental imaging trade-offs that characterize 1D lobster eye performance and must be carefully considered in optimizing the design for specific astronomical applications.

4.2 Energy-Dependent Point Spread Function Characteristics

The imaging performance of the 1D lobster eye system exhibits strong energy dependence arising from systematic variations in mirror cell contributions across the array. This creates a fundamental trade-off between effective area and angular resolution that varies continuously across the operating energy range.

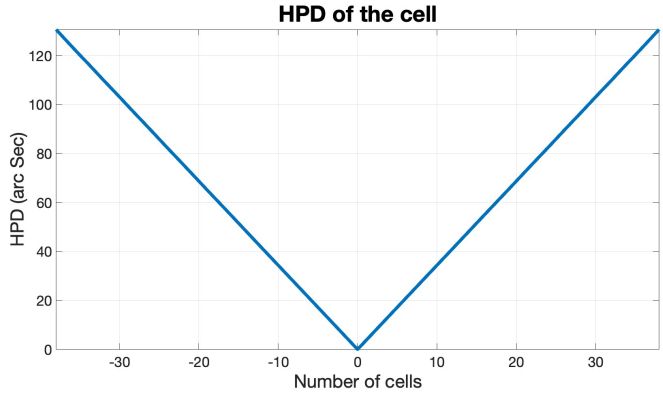

Figure 8: Half-power diameter (HPD) contribution from individual mirror cells as a function of position relative to the optical axis. The symmetric V-shaped profile shows minimal HPD at the optical axis with systematic increase for cells positioned farther from the center.

Figure 8 demonstrates the systematic variation in HPD contribution across the mirror array. The center cell provides minimum HPD contribution, while cells farther from the axis exhibit symmetric increases in imaging blur. This V-shaped profile directly reflects the geometric constraints of using flat mirror elements in spherical arrangement. The competing effects create distinct mirror cell regimes: cells close to the optical axis provide smaller effective area but larger spectral bandwidth and superior imaging performance, while cells farther from

the axis offer larger effective area but smaller bandwidth and poorer imaging performance. This systematic trade-off produces energy-dependent imaging behavior where lower energies exhibit poorer angular resolution and higher energies achieve better resolution.

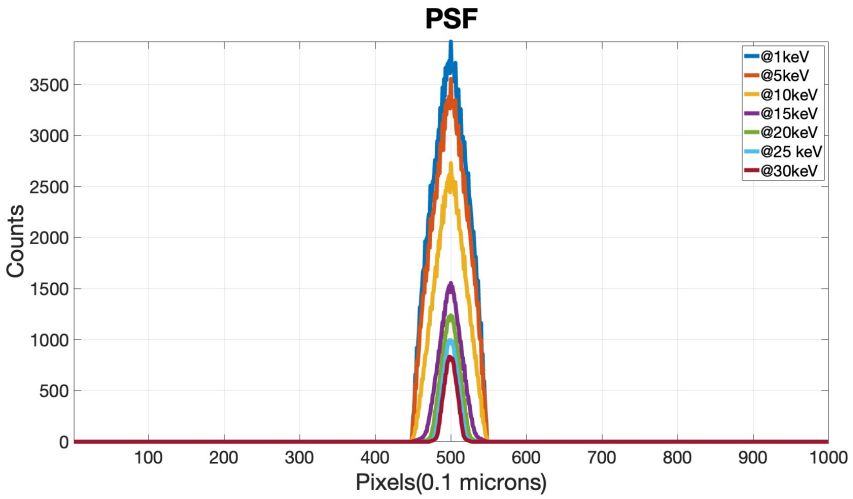

Figure 9: Simulated on-axis point spread functions for different photon energies assuming uniform source flux of 100 photons/second/cm^2. Low energies show high count rates with broader PSF, while high energies show reduced count rates with sharper PSF.

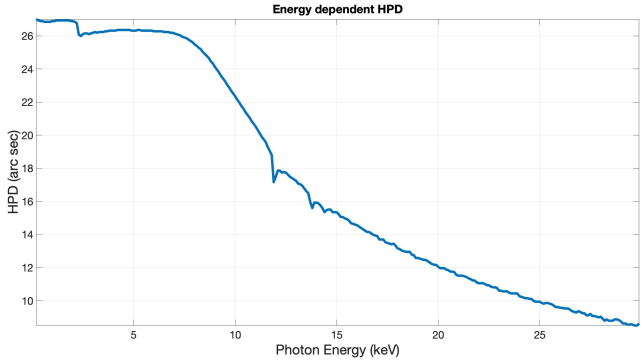

Figure 10: Energy-dependent evolution of half-power diameter for on-axis sources, showing systematic improvement in angular resolution with increasing photon energy.

Figure 9 illustrates this behavior through simulated PSF profiles sampled at 0.1 micron resolution. At 1 keV, the PSF exhibits high count rates but substantial broadening from full-array contributions. As energy increases to 30 keV, count rates decrease due to critical angle limitations while PSF profiles sharpen as only near-axis cells contribute. Figure 10 quantifies this relationship, showing HPD evolution from approximately 27 arcseconds at low energies to 8 arcseconds at 30 keV. This profile closely resembles the inverse of the effective area curve, confirming the fundamental trade-off between collecting power and imaging quality.

The 1D imaging design creates a distinctive asymmetric PSF structure shown in Figure 11. The imaging axis exhibits focused resolution determined by mirror cell contributions, while the non-imaging axis shows uniform distribution where the imaging pattern repeats to maximize collecting area. This asymmetric structure enables source localization along the imaging axis while preserving maximum sensitivity through extended collection area in the orthogonal direction.

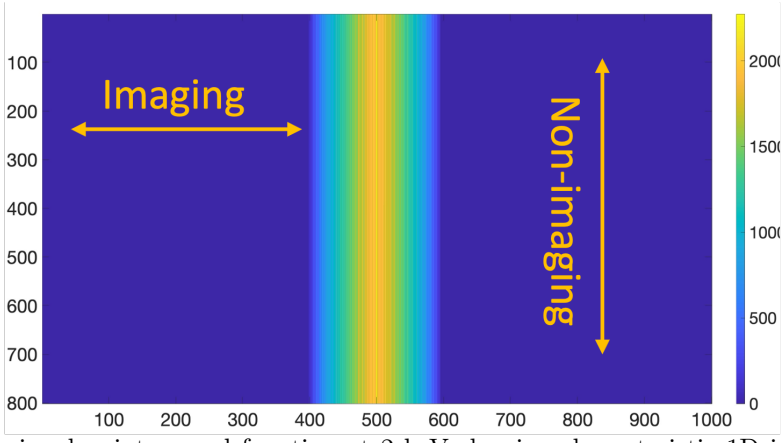

Figure 11: Two-dimensional point spread function at 2 keV showing characteristic 1D imaging behavior. The PSF exhibits focused resolution along the imaging axis (horizontal) while the non-imaging axis (vertical) simply repeats this pattern to maximize collecting area.

5. EFFECT OF IMPERFECTIONS ON IMAGING QUALITY

The ray-tracing framework provides a powerful capability to evaluate both ideal system performance and the impact of real-world imperfections on imaging quality. This methodology enables detailed error budget allocation to achieve the target sub-5 arcminute resolution requirement by systematically analyzing the effects of mirror surface errors, alignment errors, and deformations due to structural and thermal variations. The ray-trace tool directly incorporates measured surface characteristics and finite element analysis data to predict performance degradation from various error sources.

We have identified several flat mirror candidates suitable for this application and conducted high-resolution surface characterization using interferometry imaging. This metrology provides detailed surface topography data for both front and back surfaces of individual mirror elements, capturing the actual imperfections that affect optical performance. The measured surface data can be directly incorporated into the ray-tracing code to quantify the impact of mirror imperfections on half-power diameter and overall imaging quality. This approach enables selection of only those mirrors that contribute acceptably small portions of the HPD error budget toward meeting the 5 arcminute requirement.

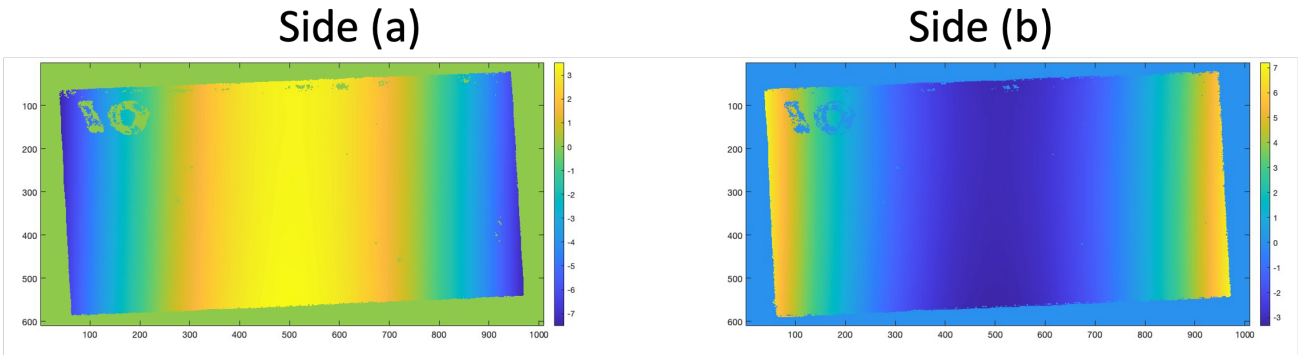

Figure 12: Surface metrology measurements from interferometry characterization showing typical mirror imperfections on both sides (a) and (b) of a representative mirror element. The surface variations exhibit characteristic patterns in both imaging and non-imaging directions that directly impact the PSF characteristics.The color bar scale is presented in microns.

Figure 12 presents an example of the comprehensive metrology scans conducted on mirror samples. The interferometry measurements reveal surface imperfections on both imaging and non-imaging axes, with charac-

teristic amplitude and spatial frequency content that varies across individual mirror elements. After measuring a representative set of mirrors, this surface data is randomly assigned to mirrors throughout the optical stack to simulate realistic performance under actual manufacturing conditions. The measured surface variations typically range from several nanometers to tens of nanometers RMS, with correlation lengths spanning from micrometers to millimeters depending on the fabrication process and handling procedures.

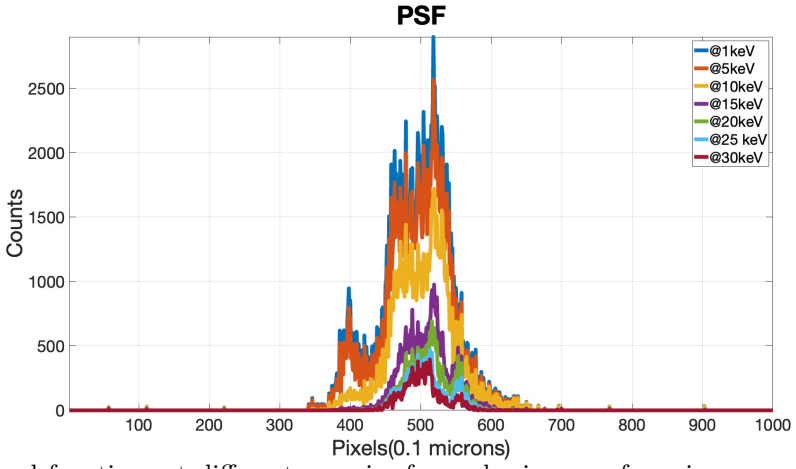

Figure 13: Point spread functions at different energies for real mirror surfaces incorporating measured surface imperfections. The energy-dependent PSF evolution shows additional broadening compared to ideal surfaces due to scattering from surface irregularities.

Figure 13 demonstrates the PSF characteristics at the center of the field for different energies when incorporating real mirror surface profiles measured from the sample shown in Figure 12. The energy-dependent PSF evolution exhibits additional broadening compared to ideal surfaces due to scattering effects from surface irregularities. Figure 14 quantifies the impact of mirror surface imperfections on imaging performance through both energy-dependent HPD analysis and two-dimensional PSF visualization. Panel (a) shows the HPD variation as a function of energy with multiple traces corresponding to different positions in the non-imaging plane. The spread in these traces directly reflects the surface imperfections in the non-imaging direction, where an ideal mirror would produce identical HPD values across all positions. The systematic variation demonstrates how surface irregularities break the perfect symmetry expected in the non-imaging axis and introduce position-dependent imaging quality. Panel (b) presents the two-dimensional PSF at 2 keV, clearly showing asymmetric broadening in the non-imaging direction that results from mirror surface imperfections. This asymmetry represents a significant departure from the ideal case where the non-imaging axis should simply repeat the imaging axis profile, confirming the importance of surface quality control in achieving target imaging performance.

6. ALIGNMENT TOLERANCE ANALYSIS

The 1D lobster eye configuration requires precise assembly of over one thousand mirror elements in an accurate spherical grid arrangement. The imaging performance of this system is inherently susceptible to mirror alignment errors, making alignment tolerance analysis critical for establishing realistic manufacturing and assembly requirements. Using ray-trace simulations, we systematically studied the effects of alignment errors on imaging performance to establish error budgets and guide precision assembly procedures.

The design requirement for our instrument specifies alignment tolerances under 1 arcminute to achieve the target imaging performance. To evaluate this requirement, we implemented random mirror tilts in both imaging and non-imaging axes within the range of ± 1 arcminute, representing realistic assembly precision achievable with careful manufacturing processes. This tolerance analysis provides quantitative guidance for assembly procedures and establishes the relationship between alignment precision and imaging quality degradation.

Figure 15 demonstrates the effects of random mirror tilts in the imaging plane. Panel (a) shows the resulting PSF with characteristic broadening in the imaging direction, where the peak broadening signature clearly

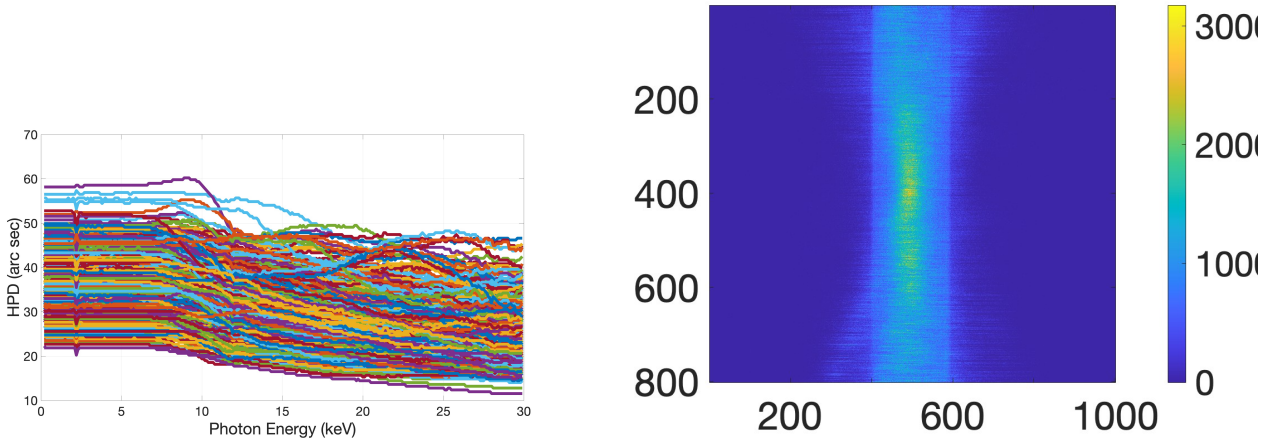

(a) (b)

Figure 14: Impact of mirror surface imperfections on imaging performance. (a) HPD variation as a function of energy showing multiple traces corresponding to different positions in the non-imaging plane. (b) Two-dimensional PSF at 2 keV showing asymmetric broadening in the non-imaging direction due to mirror surface imperfections.

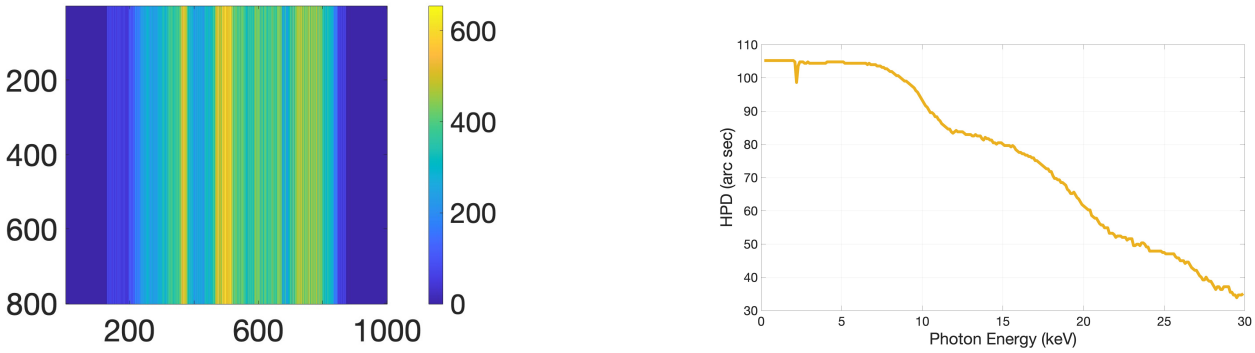

(a) (b)

Figure 15: Effect of ±1 arcminute random tilts in the imaging plane on system performance. (a) Two-dimensional PSF showing characteristic broadening in the imaging direction due to alignment errors. (b) Energy-dependent HPD demonstrating performance degradation from approximately 26 arcseconds to 105 arcseconds at low energies due to imaging-axis tilts.

indicates the effect of in-plane tilts. The asymmetric PSF structure reflects the systematic degradation caused by alignment errors that break the coherent focusing behavior. Panel (b) presents the energy-dependent HPD evolution, showing dramatic performance degradation from approximately 26 arcseconds to 105 arcseconds at low energies. This substantial degradation confirms that imaging-axis alignment represents the most critical tolerance requirement and must be controlled to maintain acceptable imaging performance.

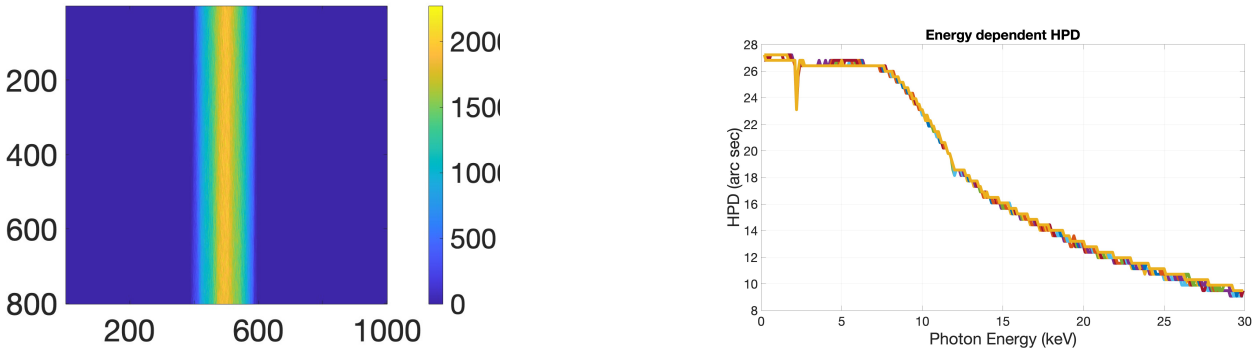

(a) (b)

Figure 16: Effect of ±1 arcminute random tilts in the non-imaging axis on system performance. (a) Two-dimensional PSF showing minimal impact on overall imaging quality with slight asymmetry in the non-imaging direction. (b) Energy-dependent HPD showing minimal degradation compared to imaging-axis tilts.

Figure 16 illustrates the effects of random mirror tilts in the non-imaging axis. The impact proves minimal compared to imaging-axis tilts, with panel (a) showing only slight asymmetry in the non-imaging direction while preserving the overall imaging quality. Panel (b) demonstrates that non-imaging axis tilts contribute only minor additions to the HPD error budget. However, these tilts break the symmetric nature of the PSF in the non-imaging axis, creating position-dependent imaging characteristics that deviate from the ideal uniform distribution expected in this direction.

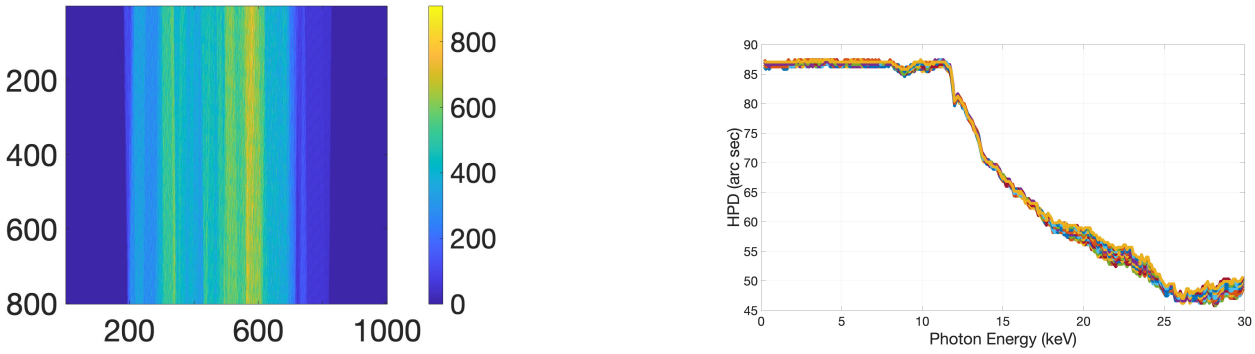

(a) (b)

Figure 17: Combined effect of ±1 arcminute random tilts in both imaging and non-imaging axes. (a) Two-dimensional PSF showing broadening in both directions with dominant degradation in the imaging axis. (b) Energy-dependent HPD reflecting the combined impact of alignment errors in both axes.

Figure 17 presents the performance characteristics when random tilts are applied in both axes simultaneously. Panel (a) shows PSF broadening in both directions, with the imaging axis continuing to dominate the overall degradation. Panel (b) demonstrates the energy-dependent HPD under combined tilt conditions, revealing how multiple error sources combine to determine the overall system performance. The combined effect shows that imaging-axis alignment remains the primary contributor to performance degradation even in the presence of non-imaging axis errors.

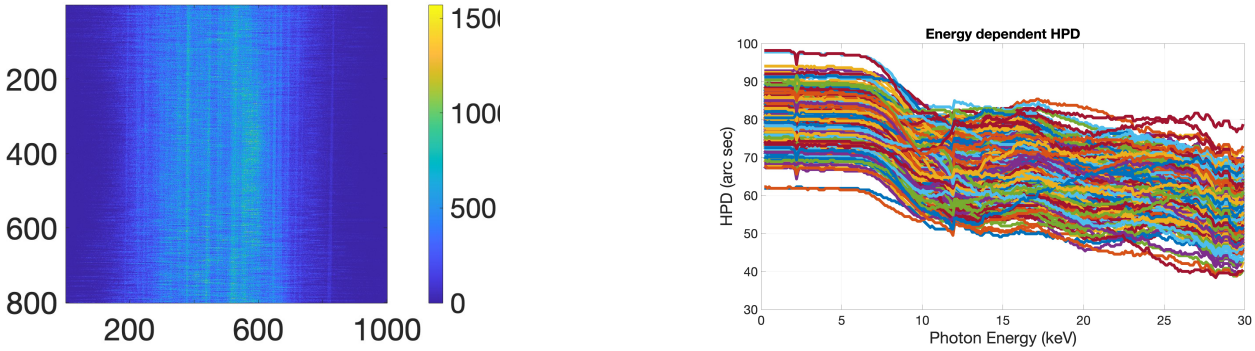

(a) (b)

Figure 18: Combined performance estimation incorporating both mirror surface imperfections and ±1 arcminute random tilts in both axes. (a) Two-dimensional PSF showing the cumulative impact of all error sources. (b) Energy-dependent HPD demonstrating the realistic system performance under combined manufacturing and alignment tolerances.

Figure 18 presents the comprehensive performance analysis incorporating both mirror surface imperfections and alignment errors. Panel (a) shows the cumulative PSF characteristics under combined error conditions, representing realistic system performance expectations. Panel (b) demonstrates the resulting energy-dependent HPD evolution, providing critical performance predictions for the complete error budget. This analysis establishes the total system performance envelope and confirms that the ±1 arcminute alignment tolerance, combined with measured mirror surface quality, enables achievement of the target imaging requirements while maintaining practical manufacturing and assembly constraints.

7. SUMMARY AND FUTURE WORK

We have presented a comprehensive design and performance analysis of a 1D lobster eye optical system optimized for wide-field X-ray transient monitoring. The design incorporates 1187 individual flat reflecting elements arranged in a cylindrical Schmidt geometry to achieve a 20.4-degree field of view with 500 mm focal length. Our systematic analysis demonstrates the fundamental trade-offs between effective area and angular resolution that characterize lobster eye optics, with the system achieving peak effective area of approximately 22 cm^2 at low energies while maintaining useful collection capability across the 1-30 keV range. The energy-dependent effective area calculations reveal how vignetting effects and critical angle limitations create wavelength-dependent performance characteristics that must be carefully considered for astronomical applications.

The imaging performance analysis reveals energy-dependent point spread function behavior where angular resolution improves from approximately 27 arcseconds at low energies to 8 arcseconds at high energies, directly reflecting the systematic variation in contributing mirror cells across the energy range. We developed a comprehensive wavelength-dependent ray-tracing framework that enables detailed performance prediction incorporating measured mirror surface characteristics, alignment errors, and geometric imperfections. This powerful simulation capability demonstrates that mirror surface imperfections introduce additional PSF broadening while alignment tolerances of ±1 arcminute significantly impact imaging quality, with imaging-axis tilts representing the dominant error source. The combined error budget analysis incorporating both surface imperfections and realistic alignment tolerances provides critical performance predictions that guide manufacturing requirements and establish achievable system specifications for transient astronomy applications.

Future development efforts will focus on expanding the performance prediction capabilities to include additional error sources that impact real-world system performance. We plan to incorporate thermal deformation effects using finite element analysis to predict temperature-induced mirror displacements and their impact on imaging quality. Structural deformation analysis will quantify the effects of gravitational loading, launch environments, and operational stresses on mirror alignment and system performance. Additionally, we will investigate coating-induced stress effects that arise from the differential thermal expansion between reflective coatings and

substrate materials, which can introduce systematic surface deformations that degrade imaging performance. These comprehensive error models will enable more accurate performance predictions and guide design optimization for space-based deployment.

We are currently developing precision alignment and mounting systems to construct the 1D lobster eye instrument with minimal systematic errors. This effort includes designing kinematic mounting interfaces that maintain mirror alignment under thermal cycling and mechanical stress while enabling efficient assembly and quality control procedures. Advanced metrology techniques are being implemented to verify mirror positioning accuracy during assembly and provide real-time feedback for alignment optimization. The mounting system development emphasizes modular construction approaches that facilitate manufacturing scalability while maintaining the stringent alignment tolerances required for target imaging performance. These technological developments will culminate in the construction and testing of a prototype system that demonstrates the feasibility of 1D lobster eye optics for wide-field X-ray transient monitoring missions.

REFERENCES

[1] Gehrels, N., Ramirez-Ruiz, E., and Fox, D. B., "Gamma-ray bursts in the swift era," in [*Annual Review of Astronomy and Astrophysics*], **47**, 567–617 (2009).

[2] Piran, T., "The afterglow - the physics of gamma-ray bursts," in [*Carnegie Observatories Astrophysics Series, Vol. 1: Coevolution of Black Holes and Galaxies*], Ho, L. C., ed. (2004).

[3] Goldstein, A., Veres, P., Burns, E., Briggs, M., Hamburg, R., Kocevski, D., Wilson-Hodge, C., Preece, R., Poolakkil, S., Roberts, O., Hui, C., Connaughton, V., Racusin, J., von Kienlin, A., Dal Canton, T., Christensen, N., Littenberg, T., Siellez, K., Blackburn, L., Broida, J., Bissaldi, E., Cleveland, W., Gibby, M., Giles, M., Kierans, C., Kouveliotou, C., McBreen, S., Mailyan, B., Meegan, C., Paciesas, W., Stanbro, M., Toelge, K., Ukwatta, T., and Yu, H.-F., "An ordinary short gamma-ray burst with extraordinary implications: Fermi-gbm detection of grb 170817a," *The Astrophysical Journal Letters* **848**(2), L14 (2017).

[4] Zhang, W. W., Peele, A. G., Petre, R., Soong, Y., and White, N. E., "Practical implementation of lobster-eye optics," in [*X-Ray Optics, Instruments, and Missions*], **3444**, 116–123, SPIE (1998).

[5] Schmidt, W., "A proposed x-ray focusing device with wide field of view for use in x-ray astronomy," *Nuclear Instruments and Methods* **127**, 285–292 (August 1975).

[6] Peele, A. G., Zhang, W. W., and Petre, R., "Mini-schmidt array for lobster-eye optics," in [*X-Ray Optics, Instruments, and Missions III*], **4012**, 432–441, SPIE (2000).

[7] Kaaret, P. and Geissbuehler, P., "Lobster-eye x-ray optics using microchannel plates," in [*Proc. SPIE 1546, Multilayer and Grazing Incidence X-Ray/EUV Optics*], 82 (1992).